

Capturing Stable HDR Videos Using a Dual-Camera System

Qianyu Zhang, Bolun Zheng*, *Member, IEEE*, Lingyu Zhu, Hangjia Pan, Zunjie Zhu,
Zongpeng Li, *Senior Member, IEEE*, Shiqi Wang, *Senior Member, IEEE*

Abstract—High Dynamic Range (HDR) video acquisition using the alternating exposure (AE) paradigm has garnered significant attention due to its cost-effectiveness with a single consumer camera. However, despite progress driven by deep neural networks, these methods remain prone to temporal flicker in real-world applications due to inter-frame exposure inconsistencies. To address this challenge while maintaining the cost-effectiveness of the AE paradigm, we propose a novel learning-based HDR video generation paradigm that decouples temporal luminance anchoring from exposure-variant detail reconstruction, overcoming the inherent limitations of the AE paradigm. To support this, we design an asynchronous dual-camera system (DCS), which enables independent exposure control across two cameras, eliminating the need for synchronization typically required in traditional multi-camera setups. Furthermore, an exposure-adaptive fusion network (EAFNet) is formulated for the DCS system. EAFNet integrates a pre-alignment subnetwork that aligns features across varying exposures, ensuring robust feature extraction for subsequent fusion, an asymmetric cross-feature fusion subnetwork that emphasizes reference-based attention to effectively merge these features across exposures, and a restoration subnetwork for final output. Extensive experimental evaluations demonstrate that the proposed method achieves state-of-the-art performance across various datasets, showing the remarkable potential of our solution in HDR video reconstruction. The codes and data captured by DCS will be available at <https://zqqqyu.github.io/DCS-HDR/>.

Index Terms—HDR video, multi-exposure image fusion, luminance alignment

I. INTRODUCTION

Capturing the full range of illumination in high dynamic range (HDR) scenarios is a challenging task for standard digital cameras [12, 21]. Thanks to the multi-exposure fusion (MEF) technology [3, 52], we can successfully capture HDR images in static scenarios by fusing multiple images of different exposure times. However, capturing HDR videos with a standard digital camera in dynamic scenes has not yet been effectively resolved [56, 57]. Early studies concentrated on designing hardware systems for directly capturing HDR video, including internal/external beam splitters [44, 55], specialized sensors [8, 18, 42], modular cameras [70] and neuromorphic cameras [17], *etc.* Although these solutions show good potential for capturing high-quality HDR videos, their high cost and bulky design severely limit their widespread adoption.

Qianyu Zhang, Bolun Zheng, Hangjia Pan, Zongpeng Li are with the School of Automation, Hangzhou Dianzi University, Hangzhou 310018, China (e-mail: qyzhang@hdu.edu.cn; blzheng@hdu.edu.cn; 1072272964@qq.com; zongpeng@tsinghua.edu.cn). Zunjie Zhu is with the Lishui Institute of Hangzhou Dianzi University (e-mail: zunjiezhu@hdu.edu.cn). Lingyu Zhu and Shiqi Wang are with the Department of Computer Science, City University of Hong Kong (e-mail: lingyzhu-c@my.cityu.edu.hk; shiqiwan@cityu.edu.hk)

The alternating exposure (AE) paradigm, first introduced by Kang *et al.* [27], enables low-cost HDR video acquisition using a single camera with rapidly switching exposures, but it also introduces challenges in maintaining temporal consistency and suppressing ghosting artifacts. Traditional AE-based methods adopt strategies such as motion-compensated fusion [16, 26] and optical flow-based reconstruction [37] to align and merge complementary exposures for HDR reconstruction, but they remain highly sensitive to motion misalignment, struggle with occlusions and non-rigid deformations, and often rely on hand-crafted heuristics that lack generalization. Recent deep learning approaches [11, 23, 62] have advanced this direction by employing deep neural architectures with stronger feature representations and learning-based alignment mechanisms. These methods have achieved promising results by training on synthetic datasets with well-structured exposure patterns and often produce temporally consistent outputs under controlled settings. However, in real-world scenarios, variations in brightness distribution caused by changes in scene content, illumination, or sensor response can disrupt the learned alignment and fusion behavior. As a result, networks that perform well in ideal conditions often suffer from temporal flickering or inconsistent reconstruction when deployed in real environments (see Fig. 1(d)).

This instability highlights a fundamental limitation of the AE paradigm itself, rather than just model design, thus leading us to explore a new solution that circumvents inter-frame exposure inconsistency. Specifically, in the AE paradigm, detail selection and global luminance determination are inherently entangled at the input level. Existing methods [11, 62] typically process both aspects within a single modeling stream, without explicit disentanglement in input design or feature representation. As a result, the network must simultaneously decide which regions to source from each exposure and how to establish the overall luminance mapping within the same representational space. As shown in Fig. 1, this tight coupling leads to feature interference and makes the learned mapping strongly dependent on the exposure patterns seen during training, thereby reducing robustness and temporal stability under distribution shifts. To address this, we propose a dual-stream generation paradigm that decouples temporal luminance anchoring from exposure-variant detail reconstruction, thereby reducing feature interference and enhancing generalization across varying exposure patterns and scene conditions. Our paradigm is meticulously designed at both the hardware system and algorithmic levels, forming a complete HDR video generation solution that supports practical deployment and robust reconstruction in real-world environments.

Our hardware architecture is designed to implement an asynchronous dual-camera system (DCS) that capitalizes on

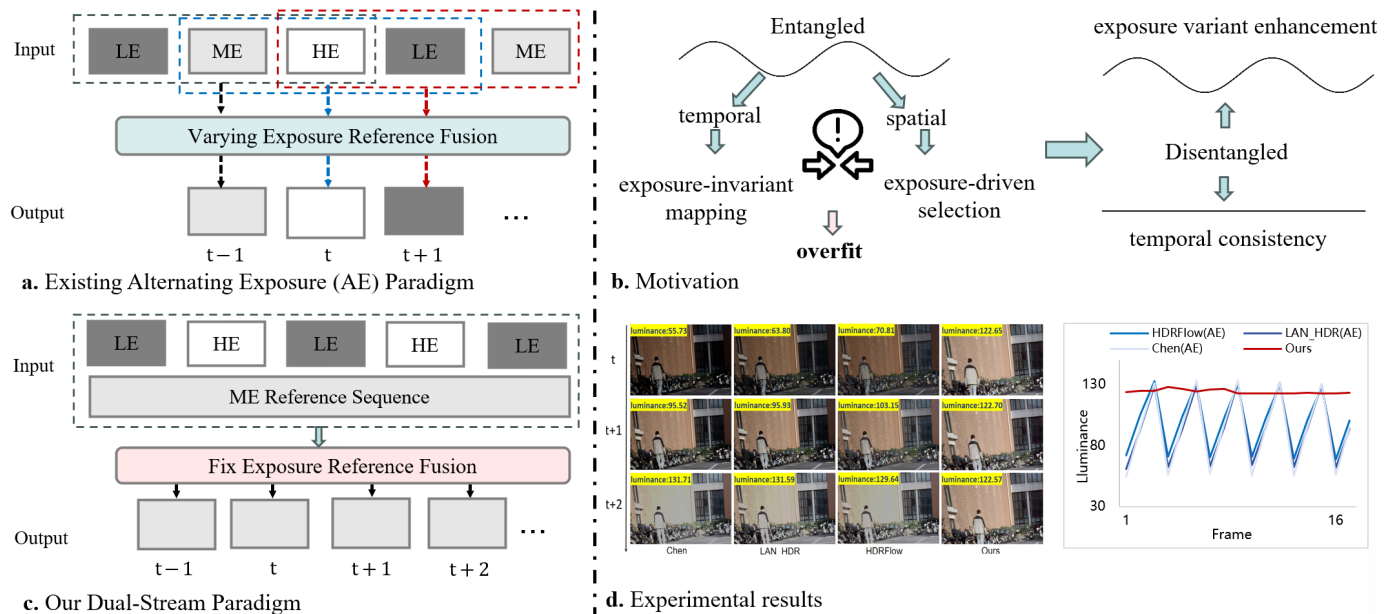


Fig. 1: Overview of the alternating exposure (AE) paradigm and our proposed dual-stream paradigm. (a) existing AE paradigm fuses alternating exposures (LE/ME/HE) with varying reference frames, resulting in flickering artifacts (luminance fluctuations exceeding 30). (b-d) Our dual-stream paradigm employs a fixed-exposure reference sequence for stable luminance anchoring, while a separate stream handles exposure-variant enhancement, ensuring consistent illumination across reference frames, enabling temporally consistent HDR reconstruction results (luminance fluctuations limited to under 1).

the prevalent availability of multi-camera hardware in consumer electronic devices. Unlike prior dual-camera HDR imaging systems [13, 32] designed for static scenes under strict synchronization constraints, our DCS is tailored for dynamic video scenarios. By relaxing the synchronization requirement, it supports independent exposure control across two cameras. This design not only facilitates flexible and practical deployment without precision alignment but also avoids the frame rate bottleneck imposed by long-exposure frames in synchronized systems. As a result, our system enables high-quality HDR video capture at high frame rates. Specifically, the designed DCS system utilizes a fixed-exposure reference sequence as the temporal baseline, while simultaneously leveraging a varying-exposure stream to enrich the dynamic range. This system-level approach addresses key limitations of existing video methods. The reference stream mitigates the temporal inconsistencies and flickering commonly observed in AE-based single-camera systems, while the division of labor between the two cameras eliminates the need for precise synchronization inherent in traditional multi-camera systems, allowing for independent and flexible exposure control. Furthermore, the proposed DCS remains fully compatible with most existing image HDR dehazing algorithms, enabling temporally consistent and robust HDR video reconstruction.

Building on the proposed paradigm and DCS system, we now turn to the algorithmic level. We first revisit existing HDR dehazing approaches to extract insights and expose their limitations. Current methods can be broadly divided into optical-flow-based [48, 50] and attention-based [36, 65] strategies. The former relies on optical flow to align inputs before fusion, which often suffers from low accuracy in

estimating optical flow. On the other hand, attention-based methods, while offering greater flexibility, their attention maps are typically computed only from texture and luminance cues, without explicitly leveraging exposure information. Moreover, they generally assign equal importance to reference and non-reference frames, which allows attention to be skewed by non-reference inputs in complex scenes. In our DCS, the presence of parallax introduces additional variations between inputs, making it even more important to design attention mechanisms that emphasize reference frames. Consequently, both categories exhibit limited robustness in dynamic, exposure-varying, and parallax-affected settings, where inaccurate alignment and exposure-insensitive attention lead to ghosting and color distortion. To address this, we propose an exposure-adaptive fusion network (EAFNet) tailored for the proposed DCS system to achieve robust and generalized HDR reconstruction. Our EAFNet consists of a pre-alignment subnetwork, an asymmetric cross-feature fusion subnetwork, and a restoration subnetwork. The pre-alignment subnetwork consists of a global luminance alignment (GLA) and an exposure-guided feature selection module (EFSM) to leverage exposure information, enhancing meaningful details and ensuring that the most relevant features are preserved despite varying exposure levels. The asymmetric cross-feature fusion subnetwork aims to explore reference-dominated attention maps, align cross-scale features, and integrate cross-feature information to improve the fusion. Additionally, the refined features are reconstructed by a lightweight restoration subnetwork built upon simplified blocks from existing architectures. In summary, our contributions can be summarized as follows:

- **Paradigm:** We introduce a dual-stream HDR video gen-

eration paradigm that explicitly decouples temporal luminance anchoring from exposure-variant detail reconstruction. Our approach employs a fixed-exposure stream to maintain temporal alignment across frames, while a complementary stream with varying exposures enhances the dynamic range. This design fundamentally improves temporal consistency and reconstruction stability.

- **System:** We design a dual-camera system to validate the feasibility of our proposed solution and bridge the gap between algorithmic design and practical deployment. Unlike traditional synchronized setups constrained by long-exposure frames, our system enables high-frame-rate video capture in dynamic scenes by supporting independent exposure control without requiring hardware-level synchronization. Moreover, the system seamlessly integrates with existing image deghosting methods to achieve temporally consistent video reconstruction.
- **Method:** To support our dual-camera system, we propose a novel model design, EAFNet. We leverage exposure information and explore the intrinsic properties of the images, ensuring that the most relevant features receive attention under different exposure conditions. Furthermore, we explore reference-dominated attention and effectively fuse complementary features across exposures, enabling robust representation under diverse lighting scenarios.
- **Results:** Our proposed dual-stream HDR video generation paradigm demonstrates significant advancements across multiple aspects. Through extensive experimental results, we demonstrate its effectiveness.

The rest of this article is organized as follows. Section II presents the related works. Section III introduces our dual-camera system for video HDR capturing. Section IV introduces the proposed EAFNet in detail. Section V presents the experimental results, and the conclusion is given in Section VI.

II. RELATED WORK

A. HDR Image Reconstruction.

1) *Traditional Approaches:* Traditional multi-exposure HDR image fusion approaches address the ghosting problem using two main approaches: motion-aligned-based and motion-rejection-based methods. Motion-aligned methods focus on globally aligning LDR images, followed by rejection of unaligned pixels to eliminate ghosting. Early works by Bogoni *et al.* [3] used optical flow for motion estimation, while later improvements by Kang *et al.* [27] incorporated exposure time information for enhanced alignment. Further advancements include patch-based energy minimization by Sen *et al.* [52] and luminance-based optimization by Hu *et al.* [20]. Motion-rejection methods, on the other hand, identify and exclude motion regions before fusion. Grosch *et al.* [15] and Jacobs *et al.* [22] detected motion using intensity differences and weighted variance, respectively, while He *et al.* [19] and Zhang *et al.* [68] refined motion detection with graph-cut and image gradient techniques.

2) *Deep Learning Approaches:* These approaches typically evolve from rigid motion compensation to flexible feature fusion, and recently to implicit representations.

CNN-based Alignment and Reconstruction. Early approaches focused on explicitly handling motion between frames. Kalantari *et al.* [24] pioneered the use of optical flow to register non-reference LDR images. Recognizing that traditional flow fails in saturated regions, subsequent works [48, 50] and SAFNet [30] employed deep optical flow networks to refine motion estimation. Alternatively, flow-free methods treat HDR as a direct image transformation task, employing direct feature concatenation [61, 66] or GAN-based frameworks [31, 47] to hallucinate missing details. Notably, Mattur *et al.* [43] extended this to stereo pairs for reconstruction. However, these methods often struggle with large-distance motions or severe occlusions, leading to ghosting artifacts when explicit alignment fails.

Attention Mechanisms and Emerging Representations. To overcome the limitations of rigid alignment, attention mechanisms were introduced to implicitly select and fuse beneficial features. AHDRNet [65] first utilized attention to suppress misaligned regions, while Liu *et al.* [35] introduced deformable convolutions for multi-scale alignment. Recently, Transformer-based architectures [5, 36, 54, 64] have integrated global context modeling to enhance feature representation. Beyond standard architectures, recent trends have also explored implicit neural representations [9, 60] to model continuous radiance fields for dynamic scenes. Despite these advances, most existing attention methods treat reference and non-reference features equally or lack explicit exposure modeling, which often results in suboptimal fusion in high-contrast regions dominated by reference-frame content.

B. HDR Video Reconstruction

Dedicated Hardware Solutions. Dedicated hardware solutions, such as single-pixel imaging [46], scanline exposure/ISO [8], internal [55] or external beam splitters [44], as well as residue cameras [70] and neuromorphic vision cameras [17], are capable of rapidly and efficiently generating detailed HDR images or videos on specialized devices. However, the complexity and high cost of these hardware solutions limit their widespread adoption.

Traditional Methods. Before the deep learning era, reconstruction primarily relied on aligning alternating exposure sequences. Kang *et al.* [27] pioneered this with global and local registration techniques. Subsequent works refined this via block-based motion estimation [37, 38] or adaptive weighting schemes [16] to mitigate artifacts. Li *et al.* [34] further proposed statistical methods to bypass exact alignment. However, these traditional approaches are computationally expensive and prone to visible ghosting artifacts in complex dynamic scenes.

Deep Learning Methods. Recent advancements have shifted focus to data-driven approaches. Kalantari *et al.* [23] proposed the first CNN-based framework for alternating exposure HDR video. Following this, researchers have explored various alignment strategies: *Flow and Attention-based Alignment:* HDR-Flow [62] introduced multi-scale large kernels for efficient flow estimation to handle large motions. To address flow inaccuracies, Chen *et al.* [4] integrated deformable convolutions for coarse-to-fine alignment, while LAN-HDR [10] utilized

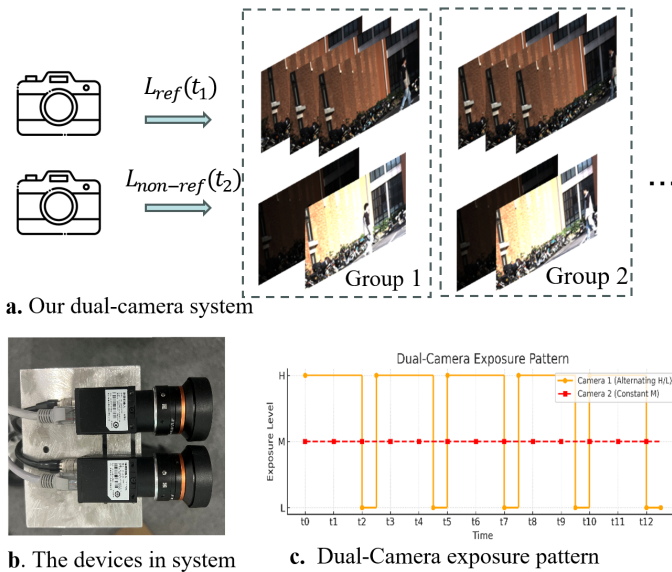


Fig. 2: Visualization of our dual-camera system. The primary camera captures continuous medium-exposure sequences as reference for temporal consistency, while the secondary camera alternates between low- and high-exposure to provide complementary information for reconstruction.

luminance-based attention to align adjacent frames with the reference. *Alternative Strategies:* Some methods attempt to bypass direct cross-exposure alignment. Khan *et al.* [28] leveraged video frame interpolation to generate intermediate frames from same-exposure inputs, thereby avoiding complex motion estimation between different exposures. Similarly, Cui *et al.* [11] treated the problem as exposure completion, employing feature interpolation to render HDR content.

Limitation of Prior Arts: Despite these improvements, a fundamental limitation remains: alternating exposure setups inherently introduce brightness inconsistencies in the reference stream (switching between short and long exposures). This leads to temporal instability and flickering. In contrast, our design adopts a fixed-exposure reference strategy, which naturally anchors brightness consistency and effectively mitigates flickering artifacts.

C. Dual-Camera Systems

Hardware-Centric and Event-Based Approaches. Early works [45] explored dual-system architectures for real-time HDR, while recent studies [2, 51] have leveraged event cameras for their superior temporal resolution. However, these hardware-centric approaches often rely on non-standard sensors or complex optical setups, limiting their widespread adoption. Consequently, the field has shifted towards deep learning-based methods using standard consumer cameras.

Dual-Camera HDR. Deep learning-based dual-camera HDR methods [13, 32] typically leverage stereo pairs to synthesize high-quality content. However, these approaches face two fundamental limitations. First, they operate under the strict assumption of 1D parallax on rectified stereo pairs. By constraining alignment to horizontal disparities, they limit their capacity

to model complex, non-rigid distortions. Specifically, motion blur in long-exposure frames creates structural inconsistencies that cannot be resolved by disparity-based alignment alone. Second, they require strict temporal synchronization. This is challenging in dynamic scenes due to exposure differences, often leading to ghosting artifacts. Furthermore, the frame rate in synchronized systems is bounded by the longest exposure time, making them unsuitable for high-frame-rate capture.

Dual-Camera Video Enhancement. Beyond HDR, dual-camera frameworks have been explored in related fields [6, 7, 14]. These methods typically pair a high-resolution/low-frame-rate stream with a low-resolution/high-frame-rate stream to reconstruct high spatiotemporal quality. While they exploit asymmetric spatial information, their optimization targets differ fundamentally from ours: they generally assume consistent exposure between cameras to maximize fidelity, rather than expanding dynamic range.

III. DUAL-CAMERA SYSTEM FOR CAPTURING HDR VIDEO

Overview. An inexpensive mainstream solution for HDR video reconstruction is generating video from image sequences captured at alternating exposure levels [11, 23, 62]. However, this approach inherits the exposure limitations of the reference frame, often resulting in visible artifacts and temporal flickering in the generated video, significantly constraining its practical application. To address this, we propose a dual-stream paradigm supported by a dual-camera system (as shown in Fig. 2), where the primary camera continuously captures medium-exposure frames to ensure temporal consistency, while the secondary camera captures low-exposure and high-exposure frames to provide complementary information.

A. Dual-Camera System

System Configuration. Our system employs two MV-CS032-10GC industrial cameras, which provide low-level access to operational controls for precise adjustment of exposure time and shooting strategies. Both cameras are equipped with identical lenses and are mounted side by side, secured by a mechanical support structure to ensure their relative positions remain stable throughout the imaging process.

Dual-Camera Calibration. To eliminate distortion and ensure fusion, we perform camera calibration using a checkerboard pattern. Intrinsic and extrinsic parameters are computed from images captured by the dual cameras using the camera calibration toolbox [69]. The calibration parameters are then applied to register the images, resulting in the final aligned images. This reduces potential errors and improves the subsequent processing steps.

Video Capture and System Design. Our dual-camera system employs two identical cameras with resolution $w \times h$. In practical operation, the cameras are run asynchronously: one continuously records a medium-exposure reference sequence $L_{ref}(t_1)$ to provide temporally consistent baseline frames, while the other alternates between low and high exposures $L_{non-ref}(t_2)$ to supply the luminance diversity required for dynamic range expansion. To leverage the information from

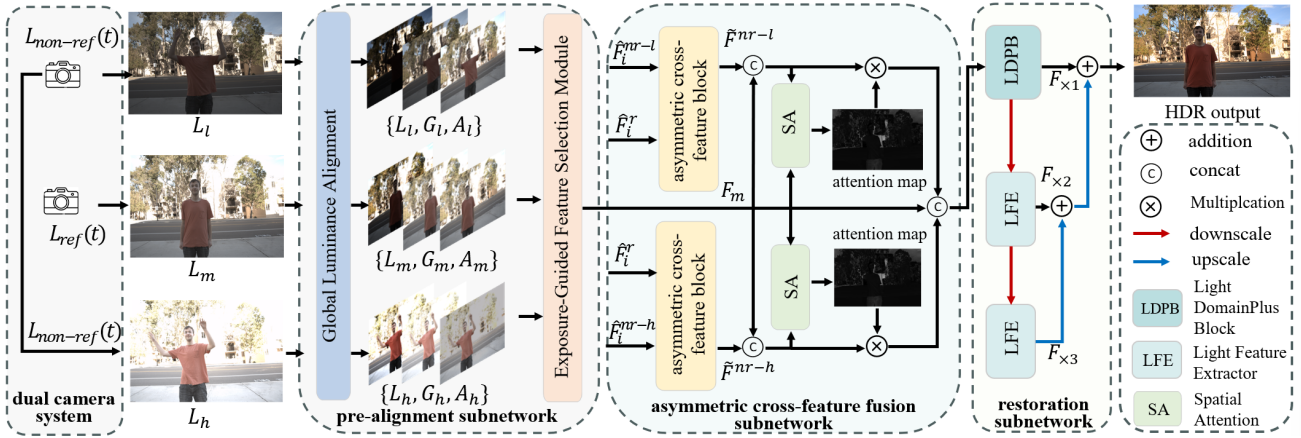


Fig. 3: The architecture of EAFNet consists of a pre-alignment subnetwork, an asymmetric cross-feature fusion subnetwork, and a restoration subnetwork. We introduce GLA and EFSM to leverage exposure information, explore the intrinsic properties of the images, and help preserve finer details across varying exposures. The asymmetric cross-feature fusion subnetwork improves image fusion by aligning cross-scale features and performing cross-feature fusion. The restoration subnetwork adopts a multi-scale architecture to reduce ghosting and refine features at different resolutions.

two sequences, we construct approximate pairings using timestamp metadata: as shown in Fig. 2(a), for each low/high exposure pair in the alternating stream, we gather reference frames falling within its defined temporal neighborhood and combine each of them with the same low/high pair to form input groups, enabling the reuse of one low/high pair across multiple reference frames. This pairing does not require frame-level precision, as the scenes are inherently dynamic and minor temporal offsets have a negligible impact on multi-exposure fusion. Each input group is then fed into the network to reconstruct HDR video at the same frame rate as $L_{ref}(t_1)$.

Overall, the design formulates the task as multi-exposure fusion for dynamic scenes, leveraging the consistent exposure of the reference sequence to eliminate the need for luminance alignment between neighboring frames. Existing HDR image dehazing methods can be seamlessly extended to achieve consistent luminance results. To address challenges from video data and the variability of real-world scenes, we propose EAFNet, a more robust network, detailed in Section IV.

B. Further Discussion

The proposed paradigm offers several distinct advantages.

First, the dual-stream design introduces an exposure-asymmetric configuration that explicitly decouples temporal stability from exposure diversity, thereby alleviating the feature interference inherent in AE-based HDR systems. Building upon this decoupling, the paradigm achieves strong scalability and generalization, allowing multi-exposure fusion models trained on public datasets to be directly applied without device-specific retraining, enabling plug-and-play deployment.

Second, it offers operational flexibility through its inherent tolerance to hardware asynchrony. Unlike synchronized systems that require precise trigger signals, our robust fusion mechanism enables the auxiliary stream to provide complementary dynamic range information regardless of its temporal phase relative to the reference stream. This relaxes strict sensor

timing constraints and simplifies hardware deployment. Furthermore, by anchoring the output frame rate to the reference stream, the system can deliver high-frame-rate HDR video while the auxiliary stream operates at a lower rate with preset exposures. Such a design improves energy efficiency and reduces bandwidth and storage overhead, enabling seamless integration with standard video encoding protocols.

Finally, our paradigm extends naturally to mobile devices featuring homogeneous dual-camera arrays, potentially offering superior efficacy compared to our prototype. On the one hand, the compact baseline of mobile cameras (approx. $1 \sim 2$ cm) is significantly smaller than that of our prototype (40 mm), naturally mitigating the parallax challenges analyzed in Sec. V-D. On the other hand, our asynchronous design circumvents the strict synchronization constraints often hindered by mobile OS latencies. Crucially, this paradigm allows mobile ISPs to leverage our dual-stream protocol to feed existing alignment methods.

IV. METHOD

A. Overview

In this section, we introduce the overall framework of the proposed EAFNet, built upon a pre-alignment subnetwork (in Sec. IV-B), an asymmetric cross-feature fusion subnetwork (in Sec. IV-C) and a restoration subnetwork (in Sec. IV-D).

As shown in Fig. 3, the pre-alignment subnetwork aims to improve detail preservation and color accuracy by exploring exposure information and extracting meaningful features from the non-reference image. It incorporates Global Luminance Alignment (GLA) to ensure consistent brightness across varying exposures, and an Exposure-guided Feature Selection Module (EFSM) to identify and focus on the most relevant regions based on the exposure information. These mechanisms work together to enhance the input features before fusion. Next, the asymmetric cross-feature fusion subnetwork plays a critical role in blending features from different exposures

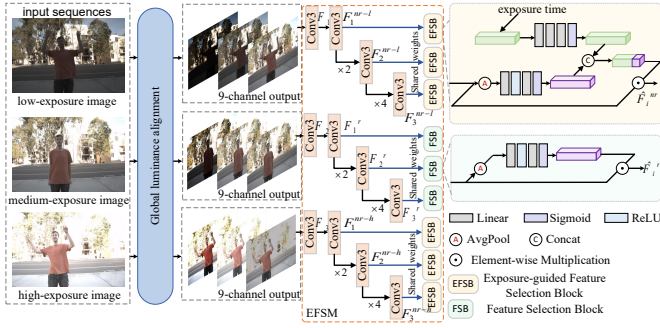


Fig. 4: The pre-alignment subnetwork is composed of two parts: global luminance alignment (GLA) and exposure-guided feature selection module (EFSM). The input is divided into multiple scales using a 3×3 convolution, with a shared-weight feature selection block applied at each scale.

while emphasizing the most important details. It processes the low- and high-exposure inputs through separate asymmetric cross-feature fusion blocks, each built with a multi-scale design. The fusion is driven by an Asymmetric Cross-Attention (ACA), which leverages reference-dominated attention maps to improve the alignment of query and key features, facilitating more effective feature propagation across multiple scales. Finally, the restoration subnetwork addresses common issues such as ghosting artifacts. It is designed to suppress ghosting while preserving fine details at multiple scales.

B. pre-alignment subnetwork

The pre-alignment subnetwork aims to extract meaningful details from the non-reference image by leveraging exposure information. GLA is introduced to maintain consistent luminance across varying exposures, while the EFSM explores the correlation between inputs and exposure to focus on the most relevant regions for fusion.

Global Luminance Alignment (GLA). Following established HDR reconstruction pipelines [25, 65], we employ three LDR images $\{L_l, L_m, L_h\}$ (sorted by their exposure length) as input. These images are first mapped to the HDR domain relying on gamma correction [25] to produce a set of gamma-corrected images G_i , where $i \in \{l, m, h\}$ and $\gamma = 2.2$.

To reduce inter-exposure luminance discrepancies and improve alignment robustness, we introduce GLA in the pre-alignment stage. GLA operates in the sRGB domain and ensures consistent luminance distributions across inputs and minimizes exposure-induced mismatches during fusion. Formally, for each non-reference LDR image L_i , global alignment is performed as:

$$A_i = \text{clip}\left(L_i \times \frac{\mathbb{E}(L_m)}{\mathbb{E}(L_i)}, 0, 1\right), \quad i \in \{l, h\}, \quad (1)$$

where A_i denotes the luminance-aligned image, $\mathbb{E}(\cdot)$ computes the average luminance, and $\text{clip}(\cdot, 0, 1)$ restricts pixel values to the valid dynamic range. Since the mid-exposure image L_m serves as the reference, we set $A_m = L_m$.

As shown in Fig. 3, given a set of LDR images with varying exposure times, we construct the input tensor

$\mathbf{L}_{\text{in}} = (\{L_l, G_l, A_l\}, \{L_m, G_m, A_m\}, \{L_h, G_h, A_h\})$, where each triplet (L_i, G_i, A_i) represents the original, gamma-corrected, and GLA-processed versions of the image under exposure setting $i \in \{l, m, h\}$. This tensor is then passed to the EFSM for feature selection and alignment refinement.

Exposure-guided Feature Selection Module (EFSM). Exposure information is crucial for distinguishing the reliability and detail across different exposures. For the obtained multi-channel features, we propose the EFSM, which consists of the Exposure-guided Feature Selection Block (EFSB) and the Feature Selection Block (FSB). EFSM introduces exposure-aware modulation based on relative exposure priors, selectively emphasizing well-exposed regions and suppressing unreliable features, thereby ensuring more reliable feature representation for fusion.

Specifically, EFSM operates in a multi-scale feature refinement architecture, as depicted in Fig. 4. Given a 9-channel composite input tensor \mathbf{L}_{in} , we first extract three initial feature maps $\{\mathbf{F}_l, \mathbf{F}_m, \mathbf{F}_h\}$ via parallel 3×3 convolutional layers. For subsequent processing clarity, we formally define $\mathbf{F}^{nr} \triangleq \{\mathbf{F}_l, \mathbf{F}_h\}$ as non-reference features and $\mathbf{F}^r \triangleq \mathbf{F}_m$ as reference features. These are fed into two distinct but weight-shared selection blocks: EFSB for non-reference features and FSB for reference features.

To encode exposure priors, we normalize the exposure times $\{t_l, t_m, t_h\}$ relative to the middle exposure as:

$$e_l = \log_2\left(\frac{t_l}{t_m}\right) \cdot c, \quad e_h = \log_2\left(\frac{t_h}{t_m}\right) \cdot c, \quad (2)$$

where e_l and e_h represent the relative exposure embeddings for the low- and high-exposure branches, respectively, and c is a hyper-parameter empirically set to 0.1.

Both \mathbf{F}^r and \mathbf{F}^{nr} are processed through global average pooling followed by two fully-connected layers and a sigmoid activation, producing feature-based modulation vectors: $\mathbf{v}^{nr} \in \mathbb{R}^{1 \times 1 \times 64}$ and $\mathbf{v}^r \in \mathbb{R}^{1 \times 1 \times 64}$. In parallel, the exposure inputs e_l, e_h are passed through a shared fully-connected layer to obtain exposure-based modulation vectors $\mathbf{v}^t \in \mathbb{R}^{1 \times 1 \times 128}$. To combine feature reliability and exposure priors, we compute the exposure-guided modulation weights as:

$$\mathbf{u}^{nr} = \sigma(\text{FC}_3([\mathbf{v}^{nr}; \mathbf{v}^t])), \quad (3)$$

where $[\cdot; \cdot]$ denotes channel-wise concatenation, $\sigma(\cdot)$ is sigmoid activation, and $\text{FC}_3(\cdot)$ represents three fully-connected layers. Finally, the refined features are obtained as:

$$\hat{\mathbf{F}}_i^r = \mathbf{F}_i^r \odot \mathbf{v}^r, \quad \hat{\mathbf{F}}_i^{nr} = \mathbf{F}_i^{nr} \odot \mathbf{u}^{nr}, \quad (4)$$

where \odot denotes element-wise multiplication.

C. asymmetric cross-feature fusion subnetwork

Leveraging non-reference details without ghosting is a critical challenge in dynamic scenes [36, 67]. We propose an asymmetric cross-feature fusion subnetwork centered on the Asymmetric Cross-Attention (ACA) module. Instead of relying on rigid local alignment, ACA reformulates the problem as global feature retrieval to select and aggregate reliable features. By leveraging multi-scale window-based attention, it captures

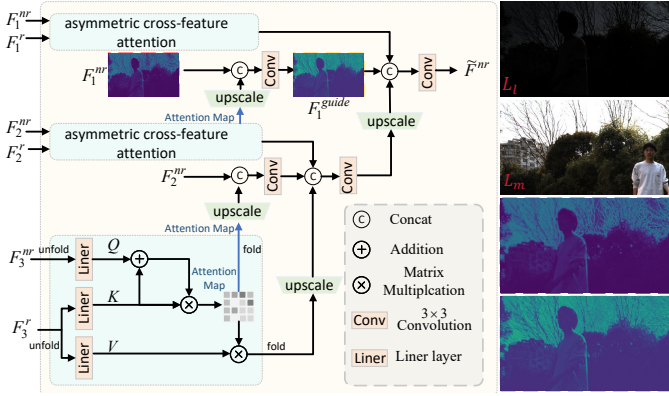


Fig. 5: The structure of the asymmetric cross-feature fusion block. It employs asymmetric cross-feature attention to align reference and non-reference features, integrating coarse-to-fine guidance for enhanced reference-dominated feature fusion and improved HDR reconstruction.

long-range dependencies, effectively handling significant spatial offsets. Furthermore, a reference-dominant mechanism strictly anchors the fusion to the reference stream, preventing artifact propagation.

As illustrated in Fig. 5, the proposed module adopts a multi-scale architecture, where local attention at each level is computed via an ACA mechanism. To mitigate feature misalignment caused by large motion, we propose an asymmetric attention mechanism that incorporates a structural prior into the matching process. Let \mathbf{F}^{nr} and \mathbf{F}^{r} denote the non-reference and reference features, respectively. We formulate the query \mathbf{Q} from the non-reference stream and the key \mathbf{K} from the reference stream. Unlike standard cross-attention, we explicitly inject reference features into the query projection to regularize the attention distribution:

$$\mathbf{M}_i = \text{softmax}\left(\frac{(\mathbf{Q}_i + \mathbf{K}_i)\mathbf{K}_i^\top}{\sqrt{C}}\right), \quad (5)$$

where $\mathbf{Q}_i = \phi(\hat{\mathbf{F}}_i^{\text{nr}})\mathbf{W}_i^q$ and $\mathbf{K}_i, \mathbf{V}_i = \phi(\hat{\mathbf{F}}_i^{\text{r}})\mathbf{W}_i^{k,v}$, with $\mathbf{W}_i^{q,k,v}$ being learnable projection matrices. This formulation reveals an implicit competition mechanism between cross-correlation and self-correlation. In aligned regions, the cross-term dominates, capturing correspondence. However, in occluded or misaligned regions where \mathbf{Q} and \mathbf{K} diverge, the cross-term vanishes. Consequently, the self-correlation term dominates the attention landscape. This acts as a fallback regularization, anchoring the attention weights to the reliable reference structure and effectively suppressing ghosting artifacts arising from the non-reference stream.

Then, the aligned non-reference features $\mathbf{F}_i^{\text{anr}}$ are obtained by applying a folding operation to the result of the multiplication of \mathbf{M}_i and \mathbf{V}_i . To enhance fine-scale alignment with global context, we incorporate a cross-scale guidance mechanism. Specifically, attention information from the coarser scale $i+1$ is projected and injected into the finer scale i as:

$$\mathbf{F}_i^{\text{guid}} = \text{Conv}_{3 \times 3}\left([\mathbf{F}_i^{\text{nr}}; U(\psi(\mathbf{M}_{i+1}))]\right), \quad 1 \leq i < N, \quad (6)$$

where $\text{Conv}_{3 \times 3}(\cdot)$ denotes a 3×3 convolution, N denotes the number of refinement scales, $U(\cdot)$ is pixel shuffle upsampling,

and $\psi(\cdot)$ represents the projection of attention from the coarser scale. Then, $\mathbf{F}_i^{\text{guid}}$ injects reference-dominated attention to facilitate multi-scale alignment. The output of the ACA \mathbf{F}^{nr} is computed by merging the aligned features from multiple scales, combining the finer-scale features with guidance from the coarser scales to produce a refined feature representation.

Finally, we generate a spatial attention (SA) map using $\hat{\mathbf{F}}^{\text{nr}}$ and \mathbf{F}^{ref} and get the fusion output.

D. restoration subnetwork

As shown in Fig. 3, the restoration subnetwork is designed to suppress ghosting artifacts while preserving fine details across multiple scales. Each scale begins with a Discrete Wavelet Transform (DWT) to decompose features into frequency subbands. At the lowest scale, where high-frequency details such as textures and residual motion artifacts are most prominent, we apply a Lightweight DomainPlus Block (LDPB) to perform frequency-specific corrections. The LDPB is adapted from [71] by removing dense connections to reduce complexity while retaining frequency modeling capacity.

In contrast, higher scales capture more global and low-frequency content. These layers are processed using a simple 1×1 convolution after DWT, which is sufficient for coarse structure refinement without the need for full spectral filtering. All features are subsequently reconstructed using the Inverse Wavelet Transform (IWT). The refined features from each scale are fused in a top-down manner using upsampling and residual connection to produce the final HDR output.

E. Loss Function

HDR images are typically displayed after tone mapping. To enhance training performance, we apply the μ -law transformation, as proposed in [24], to map the HDR image from the linear domain to the tone-mapped domain, thereby improving model performance during training, the μ -law transformation can be expressed as:

$$\tau(\mathcal{H}) = \frac{\ln(1 + \mu\mathcal{H})}{\ln(1 + \mu)} \quad (7)$$

where μ is a hyperparameter set to 5000.

We adopt the L1 loss as the basic loss function for pixel-wise supervision. However, relying solely on L1 loss often treats pixels independently, leading to over-smoothed results where high-frequency details are lost. To address this issue and improve the visual appearance of the restored images, we adopt the dilated advanced Sobel loss (D-ASL) [72] as an additional objective. The D-ASL utilizes dilated convolutions to expand the receptive field, allowing the network to capture multi-scale gradient information. This effectively suppresses blur artifacts and produces sharper edges and richer textures compared to the basic L1 loss. The function is defined as:

$$\text{ASL}(\hat{Z}, Z) = \frac{1}{N} \sum |\text{Sobel}^*(\hat{Z}) - \text{Sobel}^*(Z)| \quad (8)$$

$$\mathcal{D} - \text{ASL}^{\{d_1, d_2, \dots, d_n\}} = \sum_{i=1}^n \text{ASL}|_{\text{dilation_rate}=d_i} \quad (9)$$

TABLE I: Comparison results on Kalantari’s dataset and Prabhakar’s dataset. Throughout this paper, the best and second-best results of each case are highlighted in **bold red** and underlined blue, respectively.

Method	dataset setting metrics	train and test on Kalantari’s dataset					train and test on Prabhakar’s dataset				
		PSNR- μ (\uparrow)	PSNR-PU (\uparrow)	SSIM- μ (\uparrow)	SSIM-PU (\uparrow)	HDR-VDP-2(\uparrow)	PSNR- μ (\uparrow)	PSNR-PU (\uparrow)	SSIM- μ (\uparrow)	SSIM-PU (\uparrow)	HDR-VDP-2 (\uparrow)
Kalantari(17’ CGF) [25]		42.74	-	0.9877	-	60.51	35.63	-	0.9613	-	59.42
AHDRNet(19’ CVPR) [65]		43.77	36.97	0.9907	0.9833	62.30	38.61	30.88	0.9663	0.9319	61.14
Prabhakar(20’ ECCV) [49]		43.08	-	-	-	62.21	38.30	-	0.9702	-	-
HDR-Trans(22’ ECCV) [36]		44.28	<u>37.50</u>	0.9916	<u>0.9853</u>	66.03	<u>41.31</u>	34.60	<u>0.9726</u>	0.9622	<u>63.01</u>
DomainPlus(22’ MM) [71]		44.02	37.15	0.9910	0.9841	62.91	40.38	33.86	0.9698	0.9608	62.12
SCTNet(23’ ICCV) [54]		44.13	37.54	0.9916	0.9847	66.65	41.23	<u>34.63</u>	0.9724	<u>0.9647</u>	62.29
SAFNet(24’ ECCV) [30]		<u>44.61</u>	34.10	<u>0.9918</u>	0.9796	<u>66.93</u>	40.18	33.62	0.9705	0.9619	62.04
EAFNet(Ours)		44.69	37.79	0.9920	0.9857	68.35	41.80	35.29	0.9731	0.9660	63.53

TABLE II: Cross-dataset evaluation on Kalantari’s dataset and Prabhakar’s dataset.

Method	dataset setting metrics	train on Kalantari’s dataset, test on Prabhakar’s dataset				train on Prabhakar’s dataset, test on Kalantari’s dataset			
		PSNR- μ (\uparrow)	PSNR-PU (\uparrow)	SSIM- μ (\uparrow)	SSIM-PU (\uparrow)	PSNR- μ (\uparrow)	PSNR-PU (\uparrow)	SSIM- μ (\uparrow)	SSIM-PU (\uparrow)
AHDRNet(19’ CVPR) [65]		33.96	26.89	0.9601	0.9273	40.03	32.25	0.9855	0.9453
HDR-Trans(22’ ECCV) [36]		34.07	30.60	<u>0.9675</u>	<u>0.9429</u>	<u>41.38</u>	32.70	0.9890	0.9623
DomainPlus(22’ MM) [71]		32.64	27.74	0.9026	0.9417	41.15	32.82	0.9873	<u>0.9679</u>
SCTNet(23’ ICCV) [54]		33.83	27.35	0.9584	0.9427	40.88	<u>33.05</u>	<u>0.9892</u>	0.9611
SAFNet(24’ ECCV) [30]		<u>38.00</u>	<u>30.61</u>	0.9597	0.9264	40.86	28.93	0.9882	0.7741
EAFNet(Ours)		39.26	32.62	0.9707	0.9625	42.02	33.08	0.9903	0.9692

where N is the batch size of training, Z and \hat{Z} represent the groundtruth and the output image predicted by the network after the μ -law function, Sobel* denotes the advanced Sobel filtering, and $ASL|_{dilation_rate=d_i}$ denotes the ASL with a dilation rate of d_i . Following [72], we apply the reference settings where $D = \{1, 2, 3\}$ to formulate the D-ASL. Then the final loss function can be expressed as:

$$\mathcal{L}_{total} = \mathcal{L}_1(\hat{Z}, Z) + \lambda \cdot \mathcal{D} - ASL^D(\hat{Z}, Z) \quad (10)$$

where λ is set to 0.25 to balance the L1 loss and D-ASL.

V. EXPERIMENTS

We conduct extensive experiments to evaluate our dual-stream paradigm. Section V-A outlines the experimental setup. Section V-B benchmarks our method against state-of-the-art dehazing approaches, validating its single-frame fusion capability. Section V-C focuses on video reconstruction, demonstrating superior temporal consistency and flicker suppression over AE paradigms. We then analyze component contributions in Section V-E and investigate parallax robustness in Section V-D. Finally, Section V-F discusses limitations and future directions.

A. Experiment Settings

Training Details. The proposed method is implemented in PyTorch on an NVIDIA RTX4090 GPU. For the convolutional layers, we employ 64 kernels of size 3×3 with a stride of one, applying zero padding to preserve the dimensions of the resulting feature maps. The optimization is performed using the Adam optimizer [29] with an initial learning rate of 10^{-4} , and the training concludes when the learning rate reaches 10^{-6} , which typically requires approximately 72 hours. Both the LDR and corresponding HDR images are cropped into 256×256 patches. Patches are randomly rotated to avoid overfitting. The batch size is set to 16.

Datasets. High-quality HDR video datasets suitable for supervised training or frame-wise quantitative evaluation are scarce. Although a recent large-scale benchmark [53] has

been introduced to facilitate real-world HDR video evaluation, public resources with dense per-frame HDR ground truth and diverse exposure conditions remain limited. To fairly and comprehensively evaluate our method, we separate the evaluation into two complementary parts:

- **Spatial evaluation** focuses on single-frame fusion accuracy using HDR image datasets with reliable ground truth, enabling objective comparison in reconstruction quality. We assess single-frame fusion quality using two widely used HDR image datasets: Kalantari’s dataset [24] and Prabhakar’s dataset [50]. *Kalantari’s dataset* includes 74 training samples and 15 testing samples, with exposure values of $\{-2 \text{ EV}, 0 \text{ EV}, +2 \text{ EV}\}$ or $\{-3 \text{ EV}, 0 \text{ EV}, +3 \text{ EV}\}$. *Prabhakar’s Dataset* includes 466 training samples and 116 testing samples, with exposure values between -3EV and $+3\text{EV}$.
- **Temporal evaluation** focuses on luminance consistency and flicker suppression in dynamic scenes, which cannot be assessed using static image datasets. To ensure a rigorous and comprehensive evaluation, we conduct experiments using two distinct categories of data: *Public Video Benchmarks (Synthetic Data)*. Adopting the synthesis protocols from [4, 10, 62], we generated a large-scale HDR video training set based on the Vimeo-90K dataset [63]. This facilitates the retraining of image-based baselines, ensuring a fair comparison with video-based methods. All evaluations are conducted on the publicly available Cinematic Video Dataset [4]. *Self-captured Dual-Camera Test Dataset (Real-world Data)*. To validate our approach in practical scenarios, we introduced a dataset of 26 sequences captured under diverse real-world conditions. The data includes indoor/outdoor environments and day/night transitions, specifically targeting challenging cases like high-contrast motion and occlusions. Exposure settings are fixed to $(-2, 0, +2)$ or $(-1, 0, +1)$ EV to ensure sufficient exposure diversity across varying lighting conditions. By utilizing a dual-camera setup, we provide standard alternating exposure inputs for baselines while supplying

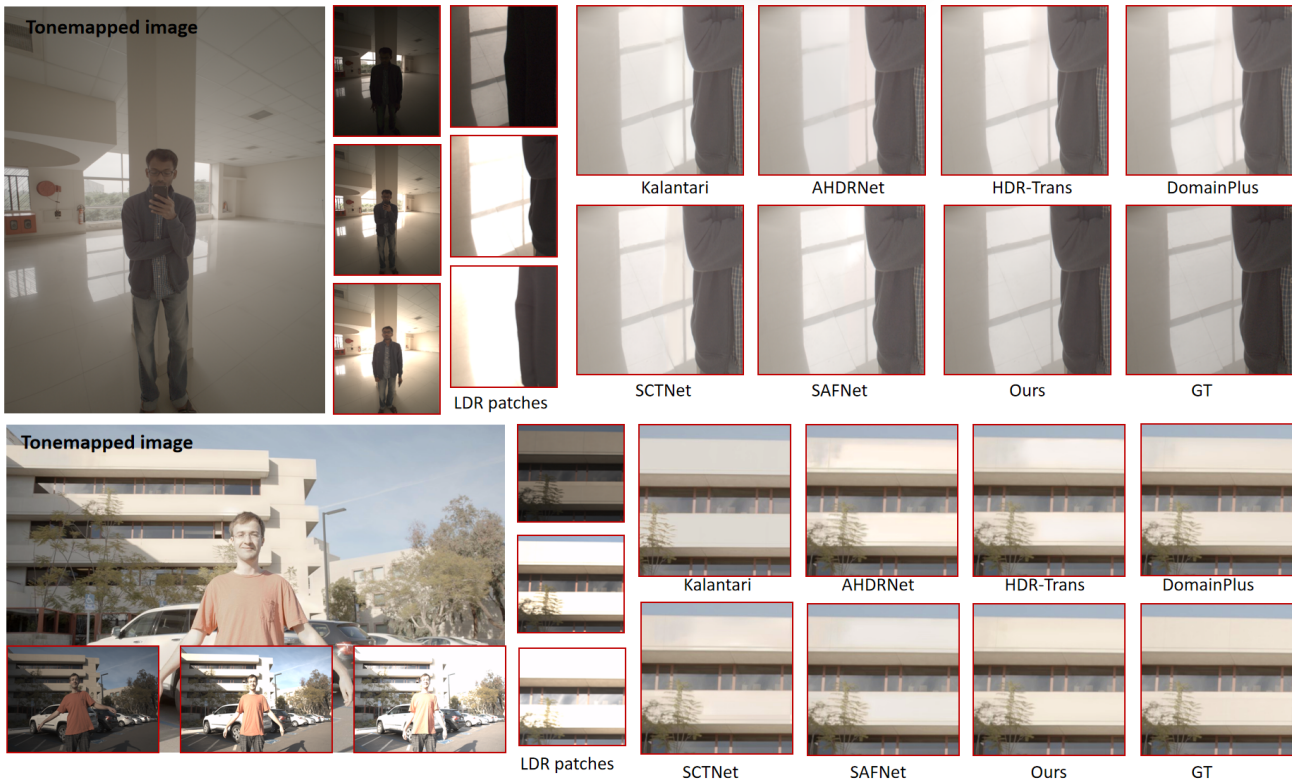


Fig. 6: Visual comparison on Kalantari’s and Prabhakar’s dataset. While other methods suffer from detail loss, overexposed patches, and color inconsistencies, our approach successfully reconstructs overexposed details and preserves natural, consistent color.

the additional medium-exposure stream for our paradigm, ensuring a fair evaluation on identical scene content.

Baselines. We compare our EAFNet to representative state-of-the-art approaches, categorized into two groups: *Multi-Exposure HDR Deghosting Methods*: We select Kalantari [25], AHDR [65], Prabhakar [49], HDR-Transformer [36], SCTNet [54], DomainPlus [71], AFUNet [33] and SAFNet [30]. *AE-based HDR video Methods*: We compare with HDR-Flow [62], LAN-HDR [10], and DeepHDRVide [4]. For fairness, we exclude few-shot and unsupervised methods that are not designed for supervised multi-exposure HDR reconstruction.

Metrics. We quantitatively evaluate the predicted HDR images by measuring PSNR and SSIM [59]. Following established protocols, we report these metrics in two domains: the tone-mapped domain ($^*-\mu$) [24] and the PU-encoded domain ($^*-\text{PU}$) [1], which is perceptually uniform and better reflects human visual response to high dynamic range content. The tone mapping operation used for evaluation is described in Sec. IV-E. Additionally, we compare the results using HDR-VDP-2 [39] for conforming the human visual perception.

To comprehensively assess video quality and temporal stability, we further employ LPIPS and temporal metrics including t-PSNR, t-SSIM [58], CVVDP [41], and FVVDP [40]. Specifically, to quantify luminance consistency and flicker, we report Luminance Standard Deviation (LSD), standard deviation of frame-wise quality metrics (STD) and Mean Absolute Difference of Brightness (MADB).

B. HDR Image Experimental Results

Quantitative Comparisons. Table I reports the intra-dataset evaluation results on Prabhakar’s and Kalantari’s datasets. Our EAFNet consistently achieves the best performance across both datasets. On the Kalantari dataset, it surpasses the second-best method by 0.08 dB in PSNR- μ , whereas on the Prabhakar’s dataset, which offers a significantly larger and more diverse evaluation set, the margin increases to 0.49 dB.

We further conduct cross-dataset validation, which is critical for evaluating the robustness of HDR fusion models against variations in exposure patterns, motion distributions, and scene content. As shown in Table II, our EAFNet maintains clear superiority in this challenging setting, with cross-domain gains even larger than in the intra-dataset case. For example, when trained on Kalantari and tested on Prabhakar, EAFNet achieves 39.26 dB PSNR- μ and 0.9707 SSIM- μ , surpassing the next best approach by over 1.2 dB and 0.03, respectively. This demonstrates that our model does not overfit to dataset-specific statistics, but learns exposure-aware and motion-robust fusion representations that transfer effectively across domains. The strong bidirectional results confirm the generality and domain-agnostic nature of our fusion mechanism.

Qualitative Comparisons. Fig. 6 presents visual comparisons on the Prabhakar and Kalantari datasets. Most existing methods exhibit noticeable ghosting artifacts, particularly around moving objects and edges with exposure differences. In overexposed regions, the Kalantari method suffers from detail

TABLE III: Quantitative comparisons of our method with other state-of-the-art methods on the Cinematic Video dataset. The values are reported in the format **Slow / Fast**, representing performance on slow-motion and fast-motion scenes, respectively.

Methods	STD (\downarrow)	PSNR_T (\uparrow)	SSIM_T (\uparrow)	HDR-VDP-2 (\uparrow)	t-SSIM (\uparrow)	t-PSNR (\uparrow)	MADB (\downarrow)	CVVDP (\uparrow)	FVVDP (\uparrow)	LPIPS (\downarrow)
DeepHDRVideo (21' ICCV)	2.70/1.12	35.60/29.60	0.8802/0.8603	66.76/59.44	0.6164/0.8092	38.79/34.08	1.22/4.30	7.22/8.02	6.67/7.89	0.3016/0.1233
LAN-HDR (23' ICCV)	2.80/ 1.07	35.75/ 31.18	0.8505/0.8536	66.53/57.85	0.6300/0.8196	39.12/ 34.59	0.90/3.07	7.71/8.16	6.95/8.00	0.2955/0.0938
HDRFlow (24' CVPR)	0.90/ 1.01	39.39/29.96	0.9000/ 0.8837	66.37/59.37	0.6813/ 0.8676	42.77/33.16	0.45/3.83	9.11/8.31	8.21/ 8.08	0.0514/ 0.0478
AHDRNet (19' CVPR)	0.49/1.14	39.68/30.27	0.9373/0.8533	63.56/61.58	0.7916/0.8358	43.86/33.57	0.12/ 1.80	8.99/8.34	7.64/7.97	0.2028/0.1242
HDRTrans (22' ECCV)	0.42/1.25	40.32/30.55	0.9412/0.8676	62.95/62.05	0.8086/0.8464	44.19/33.80	0.17/1.81	9.13/8.34	7.92/8.00	0.1036/0.1004
DomainPlus (22' MM)	0.47/1.12	40.14/30.51	0.9406/0.8665	63.39/63.06	0.8379/0.8458	44.42/33.79	0.19/1.81	9.19/8.34	8.32/8.00	0.0959/0.1005
SCTNet (23' ICCV)	0.45/1.17	39.78/30.56	0.9317/0.8752	62.61/61.93	0.8416/0.8498	44.29/33.83	0.12/1.79	9.19/8.35	8.56/7.95	0.0330/0.0554
AFUNet (25' ICCV)	0.44/1.20	40.17/30.21	0.9391/0.8663	62.89/62.69	0.8353/0.8483	44.31/33.83	0.10/1.92	9.14/8.33	7.96/7.98	0.0392/0.0768
Ours	0.39/1.23	40.87/31.12	0.9456/0.8826	63.76/63.14	0.8650/0.8604	44.95/34.30	0.11/1.79	9.32/8.44	8.56/8.03	0.0179/0.0624

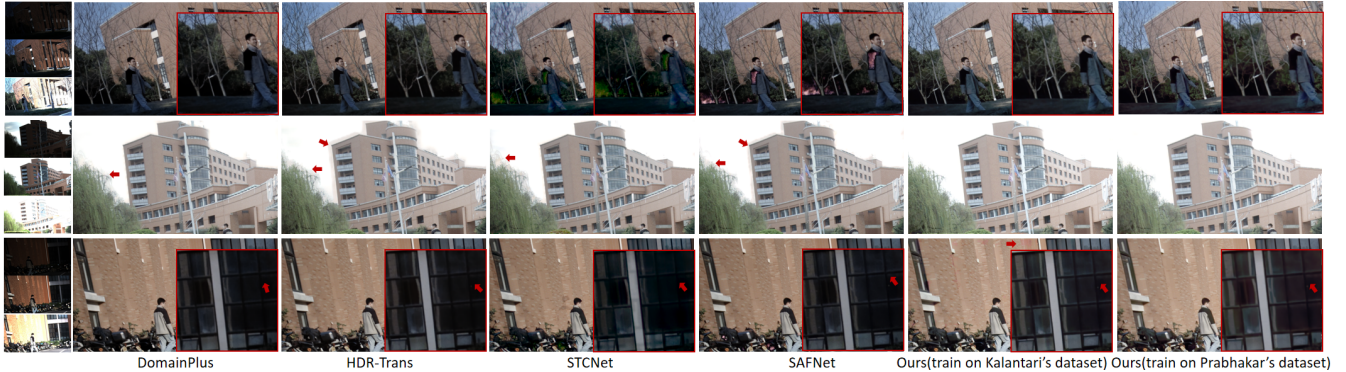


Fig. 7: Visual comparison with HDR image dehazing methods on self-captured videos. Our EAFNet reduces ghosting from motion (first row) and background misalignment (second row), recovering natural colors and fine details in dark regions (third row).

TABLE IV: Comparison on self-captured videos. * indicates HDR image dehazing methods under the alternating exposure solution. The reported time refers to the inference time for a 128×128 patch on a single RTX 4090 GPU.

Method	Paradigm	LSD (\downarrow)	t-SSIM (\uparrow)	L_{avg}	Inference time (ms)
DeepHDRVideo [4]		0.1031	0.5913	105.02	22.23
LAN-HDR [10]	alternating-exposure paradigm	0.1003	0.6879	108.75	21.69
HDRFlow [62]		0.0914	0.7352	113.49	2.62
SCTNet* [54]		0.1027	0.6947	109.23	11.17
SAFNet* [30]		0.0976	0.6862	111.70	3.27
HDR-Trans [36]	dual-stream paradigm (Ours)	0.0093	0.8923	111.24	21.60
DomainPlus [71]		0.0094	0.8991	110.41	7.44
SCTNet [54]		0.0093	0.8868	106.84	11.17
SAFNet [30]		0.0097	0.8851	111.32	3.24
EAFNet(Ours)		0.0093	0.9071	133.16	4.32

loss, while AHDRNet and HDR-Trans produce large saturated patches, and DomainPlus struggles with color inconsistencies. In contrast, EAFNet recovers fine structures in saturated areas while preserving natural and consistent color reproduction.

C. HDR Video Experimental Results

Paradigm-level comparison. The quantitative superiority shown in Table III and Table IV (e.g., lower MADB and higher t-PSNR) underscores a fundamental architectural advantage of our dual-stream paradigm over AE-based pipelines. Furthermore, as shown in Fig. 8, AE-based reconstructions suffer from severe artifacts in fast-motion scenarios: the substantial motion between alternating exposures leads to structural tearing, while the inconsistency in reference frames causes noticeable luminance fluctuations between consecutive frames.

The root cause of this performance gap lies in the stability of the reference anchor: AE methods (e.g., HDRFlow, LAN-HDR) rely on an alternating sequence. Consequently, the reference frame itself suffers from constant photometric jumping,



Fig. 8: Visual comparison with AE methods on self-captured video dataset.

The network must struggle to distinguish whether a pixel's intensity change is due to scene motion or exposure switching, leading to inevitable flickering and high STD/MADB values. In contrast, our paradigm decouples temporal stability from HDR fusion. By maintaining a continuous, fixed-exposure reference stream, we provide a luminance invariant backbone for the video. The reconstruction process is reduced to enhancing a stable video rather than stabilizing a jumping sequence. This structural guarantee allows our architecture to consistently minimize temporal fluctuations, outperforming AE baselines.

Within-dual-stream comparison. We further compare EAFNet against state-of-the-art image dehazing baselines operating under the same dual-stream framework. Note that for the Cinematic benchmark, these baselines were retrained

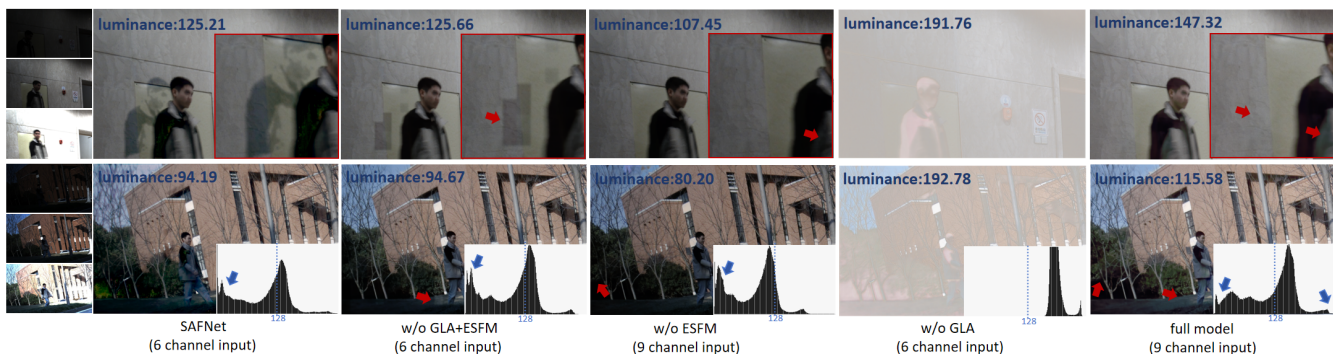


Fig. 9: Visual comparison of ablation on self-captured videos. The integration of GLA and EFSM influences the overall luminance and jointly reduces ghosting while enhancing detail in dark regions. The luminance histograms show that our method increases the visibility of extremely dark areas without causing an increase in high-luminance pixels.

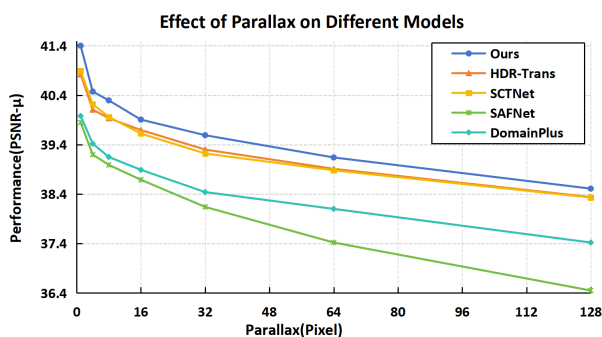


Fig. 10: Performance variation of different models under simulated parallax.

on Vimeo-90K for fair comparison.

As shown in Fig. 7, in high-motion scenarios, baselines (e.g., DomainPlus, SAFNet) often generate ghosting artifacts due to their inability to filter out misaligned features. In contrast, our ACA module effectively suppresses these parallax-induced outliers, preserving sharp spatial structures. Furthermore, under extreme luminance contrast, baselines introduce color distortions or noise in dark regions. Here, our EFSM demonstrates its robustness to exposure variation, recovering fine structures in localized low-light regions and maintaining natural transitions in overexposed areas without introducing noise. These visual improvements align with the quantitative margins in Table IV, confirming that our specialized modules handle the dual challenges of exposure disparity and spatial misalignment more effectively than generic baselines.

D. Parallax Analysis

Quantification of the Parallax Challenge. The fixed-baseline configuration of our dual-camera system inherently introduces disparity between views. Considering our hardware setup ($B \approx 44\text{mm}$ and effective focal length due to inference resizing), the disparity for a target at distance Z follows the geometric model $\Delta x \approx (f_{\text{px}}B)/Z$. Consequently, for close-range objects (e.g., 0.4m), the disparity can reach approximately 100 pixels. This poses a significant challenge for dual-camera fusion algorithms.

Comparative Stress Test. To evaluate robustness against this theoretical maximum, we conducted a controlled stress test using the 116 samples from Prabhakar’s test set. We synthetically introduced varying degrees of horizontal disparity (ranging from 0 to 100 pixels) to simulate the calculated parallax levels, comparing our method against adapted deep learning-based baselines (e.g., SAFNet, DomainPlus). As shown in Fig. 10, the performance of all methods naturally degrades as parallax increases (0 to 100 pixels) due to occlusion and information loss. However, a distinct trend is observed: CNN-based Baselines (Green Lines): Methods like SAFNet and DomainPlus exhibit a sharp drop in PSNR. These approaches rely on local receptive fields, which struggle to capture such large displacements (100 px), leading to severe ghosting artifacts when alignment fails. Transformer-based baselines (Yellow Lines): Methods like HDR-Trans and SCTNet perform better than CNNs. Thanks to the global receptive field inherent to Transformers, they can theoretically capture long-range dependencies and retrieve features across large spatial distances. Ours (Blue Line): Our method maintains the highest stability across the entire disparity range. This superior robustness stems from our unique Reference-Based Selective Fusion mechanism. Our Asymmetric Cross-Attention treats large parallax as a selection problem: When parallax is too large (e.g., occlusion), the attention module assigns low weights to the auxiliary view, effectively rejecting misaligned features. Consequently, even under extreme parallax, our failure mode is merely a local loss of dynamic range enhancement rather than the catastrophic structural destruction seen in AE-based methods.

It is worth noting that AE methods are excluded from this specific parallax analysis. Since AE methods operate on a monocular sequence, they do not suffer from spatial disparity. However, as discussed in Sec. V-C, their trade-off is extreme sensitivity to temporal motion and reference instability. Our system accepts the challenge of spatial parallax, which we solve robustly as shown above, in exchange for solving the more critical issue of temporal flickering.

E. Ablation study

In this section, we first evaluate the robustness of our framework under different dual-camera deployment conditions

TABLE V: t-SSIM comparison under different dual-camera deployment settings. **base:** Baseline dual-camera system settings. **w/o Cal.:** Dual-camera system without calibration. **Random nr.:** Randomized input order of non-reference frames. **Lower fr.:** Lower frame rate for non-reference frame input.

Method	settings	Base.	w/o Cal.	Random nr.	Lower fr.
HDR-Trans(ECCV 2022) [36]		0.8923	0.8922	0.8926	0.8924
DomainPlus(MM 2022) [71]		0.8991	0.8994	0.8997	0.8985
SCTNet(ICCV 2023) [54]		0.8868	0.8872	0.8842	0.8871
SAFNet(ECCV 2024) [30]		0.8851	0.8861	0.8848	0.8836
EAFNet(Ours)		0.9071	0.9079	0.9072	0.9066

TABLE VI: The ablation study of pre-alignment and asymmetric cross-feature fusion subnetworks on Prabhakar’s datasets

Method	pre align		fusion		PSNR- μ	PSNR-L	SSIM- μ	SSIM-L
	GLA	EFSM	ACA	<i>fguide</i>				
1	✓	✗	✓	✓	41.29	39.47	0.9728	0.9888
2	✓	✓	✗	✓	41.43	39.73	0.9722	0.9890
3	✗	✓	✓	✓	41.17	39.33	0.9726	0.9780
4	✓	✓	CA	✓	41.61	39.80	0.9726	0.9892
5	✓	✓	✓	✗	41.48	39.79	0.9723	0.9893
6	✓	✓	✗	✗	41.13	39.12	0.9708	0.9887
7	✗	✗	✗	✗	40.81	38.70	0.9703	0.9784
8	w/o. Gamma	✓	✓	✓	41.08	38.97	0.9729	0.9884
9	w/o. Origin	✓	✓	✓	41.19	39.54	0.9729	0.9882
Ours	✓	✓	✓	<i>fguide</i>	41.80	40.14	0.9731	0.9895

using our self-captured real-world dataset, focusing on the impact of calibration accuracy, input ordering, and frame rate. We then perform an ablation study on EAFNet to analyze the contribution of each component and the source of efficiency, with all results reported on Prabhakar’s dataset [50].

Dual-Camera Analysis. In a dual-camera system, imperfect calibration and potential desynchronization can lead to geometric misalignment and motion-induced misalignment, respectively. In our prototype, no special effort is made to achieve sub-pixel calibration or perfect synchronization. Instead, the fusion framework is designed to tolerate moderate deviations in both geometry and timing. The training data include dynamic scenes with motion and occlusion, allowing the model to learn robustness to such spatial inconsistencies.

Table V reports t-SSIM under four deployment variants. Variations across deployment variants are small for all methods (≤ 0.003), indicating that, within the tested range, moderate calibration errors, input order changes, and frame-rate reductions have limited impact on temporal flickering. Minor fluctuations are likely due in part to the cropping required for alignment rather than alignment failure itself. Overall, the results suggest that, within the tested range of deviations, temporal stability can be maintained without the need for precise calibration and strict synchronization, but a higher level of calibration and synchronization may still be beneficial for optimizing performance in more demanding scenarios.

Global Luminance Alignment. We alter the composition of the input channels and configure four scenarios to investigate the impact of GLA. As shown in Table VI (comparing Method 3, 8, 9, and Ours), incorporating GLA yields a substantial improvement in SSIM. By linearly aligning the intensity statistics, GLA ensures that the subsequent fusion modules rely on geometric correspondence rather than being misled by exposure discrepancies, bringing simultaneous gains in both luminance accuracy and structural fidelity.

The visualization results of the ablation experiments on

TABLE VII: Experiments on changing the proportions in exposure-guided feature selection module

Method	Proportions	PSNR- μ	PSNR-L	SSIM- μ	SSIM-L
1	1:2	41.41	39.66	0.9728	0.9791
2	1:1	41.43	39.70	0.9728	0.9892
3	4:1	41.68	40.00	0.9725	0.9893
4	8:1	41.72	40.02	0.9726	0.9894
5	w/o self content	41.37	39.61	0.9723	0.9769
6	w/o exposure time	41.52	39.86	0.9723	0.9784
Ours	2:1	41.80	40.14	0.9731	0.9895

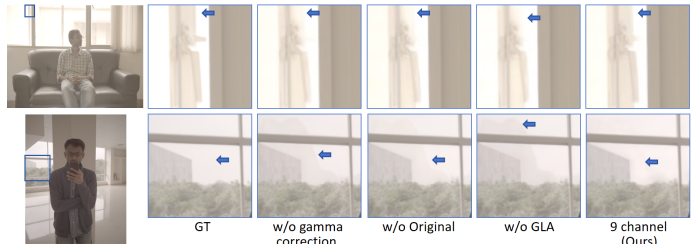


Fig. 11: The contributions of global luminance alignment.

GLA with Prabhakar’s dataset are shown in Fig. 11, in the first row, other variants fail to restore the overexposed details of the window frame. In the second row, ghosting occurs in the overexposed areas outside the window. The introduction of the global luminance alignment method leads to enhanced detail preservation while effectively mitigating undesirable artifacts. Additionally, this structural alignment serves as a prerequisite for the subsequent EFSM, enabling the full model to achieve the significant performance gains observed in Table VI.

Exposure-guided Feature Selection Module. Table VI (comparing Methods 1, 2, 3, and Ours) highlights a critical coupling between EFSM and GLA: *1. EFSM depends on GLA for Stability.* Without GLA, EFSM fails to improve performance and even causes negative optimization. Lacking a unified luminance baseline, the module misinterprets large exposure gaps as structural noise, erroneously discarding valid features. Once GLA aligns the input statistics, it unlocks the potential of EFSM, allowing it to focus on structural selection. As shown in Fig. 9, this synergy boosts PSNR- μ by 0.37 dB and significantly enhances visibility in dark regions without saturation. *2. GLA depends on EFSM for Feature Discrimination.* Conversely, utilizing GLA alone leads to feature homogenization. By globally scaling pixel intensities to match the reference, GLA can mask the intrinsic SNR advantages of auxiliary frames. For instance, when high-exposure frames are linearly down-scaled to match the reference, their clean shadow details become numerically indistinguishable from the noisy shadows of the reference. EFSM serves as a critical discriminator: it explicitly identifies and preserves these high-quality regions based on their structural richness before the network conflates them with the reference features, ensuring that the alignment process does not compromise texture recovery.

Beyond the module dependency, we observe that the efficacy of feature selection is sensitive to the ratio between feature-based and exposure-based modulation coefficients. To investigate this, we conduct an in-depth analysis on six variants (Table VII). *1) Necessity of Explicit Exposure:* Explicit exposure guidance is verified to be essential. As evidenced in Row

TABLE VIII: Performance Benchmarking of the Proposed Framework Across Different Hardware Platforms and Configurations.

Platform	Resolution	Precision	Framework	Readout* (ms)	Rectification (ms)	Inference (ms)	Tone Map (ms)	Sys Memory (MB)	FPS	Peak VRAM (MB)	Energy (J/Frame)	Power	Performance
Desktop (RTX 4090)	1080p	FP32	PyTorch	8	4	437	0.006	3902.36	2.03	13797.09	178.50	363.21	44.41
	1080p	FP16	PyTorch	8	4	251	0.006	3902.70	3.73	6962.85	96.50	359.83	44.40
	1080p	FP32	ONNX	8	4	434	0.006	3222.80	2.30	22896.01	167.42	373.90	44.41
	1080p(tiling)	FP32	PyTorch	8	4	400	0.006	3918.75	2.5	3470.36	-	-	44.30
	1080p(tiling)	FP16	PyTorch	8	4	210	0.006	3920.32	4.76	1702.42	-	-	44.30
	4K (tiling)	FP32	PyTorch	8	4	383	0.006	3918.80	2.61	3366.09	-	-	44.30
Laptop (iGPU)	1080p(tiling)	FP32	ONNX	-	-	614	-	1483.72	1.63	-	-	-	44.30
Mobile (Jetson AGX Xavier)	1080p(tiling)	FP32	ONNX	-	-	1852	-	1809.59	0.54	-	-	-	44.30

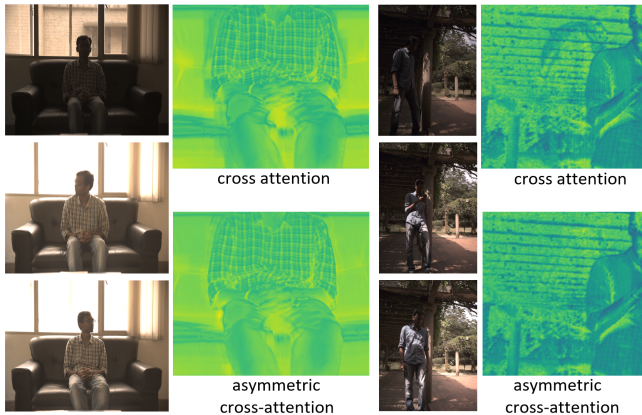


Fig. 12: Visual comparison of asymmetric cross-attention and cross-attention.

6, removing the exposure input results in a performance drop of 0.28 dB compared to our method. This quantitative gap suggests that the network struggles to accurately infer the exposure status implicitly from image data alone, likely stemming from the physical ambiguity between object reflectance and illumination. 2) *Rationale for the 2:1 Ratio*: Among the varied settings, the 2:1 ratio achieves the highest PSNR- μ . Crucially, comparisons with Rows 1 and 2 reveal that over-weighting exposure degrades performance, yielding results even lower than the version without exposure guidance. This indicates that exposure information must serve as a regulated condition rather than a dominant feature; the 2:1 ratio represents the optimal equilibrium that resolves ambiguity without interfering with feature representation.

Asymmetric Cross-feature Fusion Subnetwork. Table VI demonstrates that replacing our fusion subnetwork with a generic attention block [65] causes a 0.67 dB performance drop. Qualitative results in Fig. 13 and Fig. 12 confirm our method’s superior ghosting removal. Moreover, replacing standard Cross-Attention (CA) with our Asymmetric Cross-Attention (ACA) yields a 0.19 dB gain (line 5). This improvement stems from our reference-dominant design, which introduces a reference-based structural prior to suppress misaligned outliers. Additionally, the cross-scale guidance features f_{guide} further refine the fusion, reducing artifacts and boosting PSNR- μ by 0.32 dB.

F. limitation

Efficiency Analysis.

While our asynchronous dual-camera design resolves the acquisition bottleneck for real-time capture, the reconstruct-

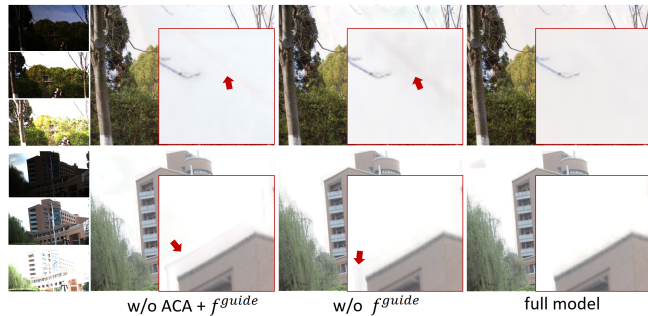


Fig. 13: Visual comparison of ablation on self-captured videos. Our method reduces most ghosting artifacts.



Fig. 14: Visualization of a failure case in an extreme contrast nighttime scene.

tion speed presents a computational trade-off. As detailed in Table VIII and Table IV, the use of Transformer-based modules for long-range dependency modeling incurs higher latency compared to lightweight CNNs. On an RTX 4090, our method achieves ≈ 4.76 FPS at 1080p using FP16 optimization. However, deployment on edge devices remains challenging; for instance, inference drops to 0.54 FPS on the Jetson AGX Xavier. Future work will focus on model compression (e.g., quantization, pruning) to bridge this gap for mobile applications.

Failure Case. One limitation of our approach is observed in nighttime scenes with extreme contrast. As shown in Fig. 14, the scene contains localized high-brightness regions (e.g., street lamps) against a nearly black background. In the reference low-exposure frame, the majority of the pixels are close to zero, providing insufficient textural cues for feature alignment, while the light sources are severely over-exposed. As a result, the network fails to properly synthesize the HDR content in these saturated areas, resulting in artifacts.

VI. CONCLUSION

In this work, we revisit the fundamental cause of temporal instability in alternating-exposure (AE) HDR video, which lies in the entanglement of temporal luminance anchoring with exposure-dependent detail selection, and propose a dual-stream paradigm that explicitly decouples these two roles. Specifically, we introduce an exposure-asymmetric dual-camera system (DCS) that fixes the reference exposure to stabilize frame-to-frame luminance while allowing the auxiliary stream to vary exposure for capturing high dynamic range details. To support this system, we design EAFNet to effectively suppress ghosting artifacts while preserving fine details in real-world scenes. Extensive experiments on multiple datasets and real-world sequences demonstrate that the proposed paradigm improves both temporal stability and reconstruction quality compared with AE-based baselines and HDR image deghosting methods, while remaining cost-efficient and deployment-friendly. Our dual-stream solution provides a promising direction for real-time HDR video capture.

REFERENCES

- [1] Maryam Azimi et al. Pu21: A novel perceptually uniform encoding for adapting existing quality metrics for hdr. In *2021 Picture Coding Symposium (PCS)*, pages 1–5. IEEE, 2021.
- [2] Yuhan Bao, Lei Sun, Yuqin Ma, and Kaiwei Wang. Temporal-mapping photography for event cameras. In *European Conference on Computer Vision*, pages 55–72. Springer, 2024.
- [3] Luca Bogoni. Extending dynamic range of monochrome and color images through fusion. In *Proceedings 15th International Conference on Pattern Recognition. ICPR-2000*, volume 3, pages 7–12. IEEE, 2000.
- [4] Guanying Chen, Chaofeng Chen, Shi Guo, Zhetong Liang, Kwan-Yee K Wong, and Lei Zhang. Hdr video reconstruction: A coarse-to-fine network and a real-world benchmark dataset. In *Proceedings of the IEEE/CVF international conference on computer vision*, pages 2502–2511, 2021.
- [5] Rufeng Chen, Bolun Zheng, Hua Zhang, Quan Chen, Chenggang Yan, Gregory Slabaugh, and Shanxin Yuan. Improving dynamic hdr imaging with fusion transformer. In *Proceedings of the AAAI Conference on Artificial Intelligence*, volume 37, pages 340–349, 2023.
- [6] Ming Cheng, Zhan Ma, M Salman Asif, Yiling Xu, Haojie Liu, Wenbo Bao, and Jun Sun. A dual camera system for high spatiotemporal resolution video acquisition. *IEEE Transactions on Pattern Analysis and Machine Intelligence*, 43(10):3275–3291, 2020.
- [7] Ming Cheng, Yiling Xu, Wang Shen, M Salman Asif, Chao Ma, Jun Sun, and Zhan Ma. H 2-stereo: High-speed, high-resolution stereoscopic video system. *IEEE Transactions on Broadcasting*, 68(4):886–903, 2022.
- [8] Inchang Choi, Seung-Hwan Baek, and Min H Kim. Reconstructing interlaced high-dynamic-range video using joint learning. *IEEE Transactions on Image Processing*, 26(11):5353–5366, 2017.
- [9] Juhung Choi, Jinnyeong Kim, Seokjun Choi, Jinwoo Lee, Samuel Brucker, Mario Bijelic, Felix Heide, and Seung-Hwan Baek. Dual exposure stereo for extended dynamic range 3d imaging. In *Proceedings of the Computer Vision and Pattern Recognition Conference*, pages 6283–6293, 2025.
- [10] Haesoo Chung and Nam Ik Cho. Lan-hdr: Luminance-based alignment network for high dynamic range video reconstruction. In *Proceedings of the IEEE/CVF International Conference on Computer Vision*, pages 12760–12769, 2023.
- [11] Jiahao Cui, Wei Jiang, Zhan Peng, Zhiyu Pan, and Zhiguo Cao. Exposure completing for temporally consistent neural high dynamic range video rendering. In *Proceedings of the 32nd ACM International Conference on Multimedia*, pages 10027–10035, 2024.
- [12] Paul E Debevec and Jitendra Malik. Recovering high dynamic range radiance maps from photographs. In *ACM SIGGRAPH 2008 classes*, pages 1–10. 2008.
- [13] Xuan Dong, Xiaoyan Hu, Weixin Li, Xiaojie Wang, and Yunhong Wang. Miehdr cnn: Main image enhancement based ghost-free high dynamic range imaging using dual-lens systems. In *Proceedings of the AAAI Conference on Artificial Intelligence*, volume 35, pages 1264–1272, 2021.
- [14] Xuan Dong, Xiangyuan Sun, Xia Wang, Jian Song, Ya Li, and Weixin Li. Video demoreing using focused-defocused dual-camera system. *IEEE Transactions on Pattern Analysis and Machine Intelligence*, 2025.
- [15] Thorsten Grosch et al. Fast and robust high dynamic range image generation with camera and object movement. *Vision, Modeling and Visualization, RWTH Aachen*, 277284(3):2, 2006.
- [16] Yulia Gryaditskaya, Tania Pouli, Erik Reinhard, Karol Myszkowski, and Hans-Peter Seidel. Motion aware exposure bracketing for hdr video. In *Computer Graphics Forum*, volume 34, pages 119–130. Wiley Online Library, 2015.
- [17] Jin Han, Chu Zhou, Peiqi Duan, Yehui Tang, Chang Xu, Chao Xu, Tiejun Huang, and Boxin Shi. Neuromorphic camera guided high dynamic range imaging. In *Proceedings of the IEEE/CVF Conference on Computer Vision and Pattern Recognition*, pages 1730–1739, 2020.
- [18] Felix Heide, Markus Steinberger, Yun-Ta Tsai, Mushfiqur Rouf, Dawid Pajkak, Dikpal Reddy, Orazio Gallo, Jing Liu, Wolfgang Heidrich, Karen Egiazarian, et al. Flexisp: A flexible camera image processing framework. *ACM Transactions on Graphics (ToG)*, 33(6):1–13, 2014.
- [19] Yong Seok Heo, Kyoung Mu Lee, Sang Uk Lee, Youngsu Moon, and Joonhyuk Cha. Ghost-free high dynamic range imaging. In *Asian Conference on Computer Vision*, pages 486–500. Springer, 2010.
- [20] Jun Hu, Orazio Gallo, Kari Pulli, and Xiaobai Sun. Hdr deghosting: How to deal with saturation? In *Proceedings of the IEEE Conference on Computer Vision and Pattern Recognition*, pages 1163–1170, 2013.
- [21] Katrien Jacobs, Celine Loscos, and Greg Ward. Automatic high-dynamic range image generation for dynamic

- scenes. *IEEE Computer Graphics and Applications*, 28(2):84–93, 2008.
- [22] Katrien Jacobs, Celine Loscos, and Greg Ward. Automatic high-dynamic range image generation for dynamic scenes. *IEEE Computer Graphics and Applications*, 28(2):84–93, 2008.
- [23] Nima Khademi Kalantari and Ravi Ramamoorthi. Deep hdr video from sequences with alternating exposures. In *Computer graphics forum*, volume 38, pages 193–205. Wiley Online Library, 2019.
- [24] Nima Khademi Kalantari, Ravi Ramamoorthi, et al. Deep high dynamic range imaging of dynamic scenes. *ACM Trans. Graph.*, 36(4):144–1, 2017.
- [25] Nima Khademi Kalantari, Ravi Ramamoorthi, et al. Deep high dynamic range imaging of dynamic scenes. *ACM Trans. Graph.*, 36(4):144–1, 2017.
- [26] Nima Khademi Kalantari, Eli Shechtman, Connelly Barnes, Soheil Darabi, Dan B Goldman, and Pradeep Sen. Patch-based high dynamic range video.
- [27] Sing Bing Kang, Matthew Uyttendaele, Simon Winder, and Richard Szeliski. High dynamic range video. *ACM Transactions on Graphics (TOG)*, 22(3):319–325, 2003.
- [28] Zeeshan Khan, Parth Shettiwar, Mukul Khanna, and Shanmuganathan Raman. Deephs-hdrvideo: Deep high speed high dynamic range video reconstruction. In *2022 26th International Conference on Pattern Recognition (ICPR)*, pages 1959–1966. IEEE, 2022.
- [29] Diederik P Kingma and Jimmy Ba. Adam: A method for stochastic optimization. *arXiv preprint arXiv:1412.6980*, 2014.
- [30] Lingtong Kong, Bo Li, Yike Xiong, Hao Zhang, Hong Gu, and Jinwei Chen. Safnet: Selective alignment fusion network for efficient hdr imaging. In *European Conference on Computer Vision*, pages 256–273. Springer, 2024.
- [31] Ru Li, Chuan Wang, Jue Wang, Guanghui Liu, Hengyu Zhang, Bing Zeng, and Shuaicheng Liu. Uphdr-gan: Generative adversarial network for high dynamic range imaging with unpaired data. *IEEE Transactions on Circuits and Systems for Video Technology*, 32(11):7532–7546, 2022.
- [32] Weixin Li, Tiantian Cao, Chang Liu, Xue Tian, Ya Li, Xiaojie Wang, and Xuan Dong. Dual-lens hdr using guided 3d exposure cnn and guided denoising transformer. *ACM Transactions on Multimedia Computing, Communications and Applications*, 19(5):1–20, 2023.
- [33] Xinyue Li, Zhangkai Ni, and Wenhan Yang. Afunet: Cross-iterative alignment-fusion synergy for hdr reconstruction via deep unfolding paradigm. *arXiv preprint arXiv:2506.23537*, 2025.
- [34] Yuelong Li, Chul Lee, and Vishal Monga. A maximum a posteriori estimation framework for robust high dynamic range video synthesis. *IEEE Transactions on Image Processing*, 26(3):1143–1157, 2016.
- [35] Zhen Liu, Wenjie Lin, Xinpeng Li, Qing Rao, Ting Jiang, Mingyan Han, Haoqiang Fan, Jian Sun, and Shuaicheng Liu. Adnet: Attention-guided deformable convolutional network for high dynamic range imaging. In *Proceedings of the IEEE/CVF Conference on Computer Vision and Pattern Recognition*, pages 463–470, 2021.
- [36] Zhen Liu, Yinglong Wang, Bing Zeng, and Shuaicheng Liu. Ghost-free high dynamic range imaging with context-aware transformer. In *European Conference on Computer Vision*, pages 344–360. Springer, 2022.
- [37] Stephen Mangiat and Jerry Gibson. High dynamic range video with ghost removal. In *Applications of digital image processing XXXIII*, volume 7798, pages 307–314. SPIE, 2010.
- [38] Stephen Mangiat and Jerry Gibson. Spatially adaptive filtering for registration artifact removal in hdr video. In *2011 18th IEEE International Conference on Image Processing*, pages 1317–1320. IEEE, 2011.
- [39] Rafał Mantiuk, Kil Joong Kim, Allan G Rempel, and Wolfgang Heidrich. Hdr-vdp-2: A calibrated visual metric for visibility and quality predictions in all luminance conditions. *ACM Transactions on Graphics (TOG)*, 30(4):1–14, 2011.
- [40] Rafał K Mantiuk, Gyorgy Denes, Alexandre Chapiro, Anton Kaplanyan, Gizem Rufo, Romain Bachy, Trisha Lian, and Anjul Patney. Fovvideovdp: A visible difference predictor for wide field-of-view video. *ACM Transactions on Graphics (TOG)*, 40(4):1–19, 2021.
- [41] Rafal K Mantiuk, Param Hanji, Maliha Ashraf, Yuta Asano, and Alexandre Chapiro. Colorvideovdp: A visual difference predictor for image, video and display distortions. *arXiv preprint arXiv:2401.11485*, 2024.
- [42] Julien NP Martel, Lorenz K Mueller, Stephen J Carey, Piotr Dudek, and Gordon Wetzstein. Neural sensors: Learning pixel exposures for hdr imaging and video compressive sensing with programmable sensors. *IEEE Transactions on Pattern Analysis and Machine Intelligence*, 42(7):1642–1653, 2020.
- [43] Shashaank A Mattur and Mohamed-Chaker Larabi. Deep high dynamic range imaging using differently exposed stereo images. In *2021 IEEE International Conference on Image Processing (ICIP)*, pages 2888–2892. IEEE, 2021.
- [44] Morgan McGuire, Wojciech Matusik, Hanspeter Pfister, Billy Chen, John F Hughes, and Shree K Nayar. Optical splitting trees for high-precision monocular imaging. *IEEE Computer Graphics and Applications*, 27(2):32–42, 2007.
- [45] Joshua McNamee, Jonathan Hatchett, Kurt Debattista, and Alan Chalmers. Live hdr video streaming on commodity hardware. In *Applications of Digital Image Processing XXXVIII*, volume 9599, pages 278–288. SPIE, 2015.
- [46] Shree K Nayar and Tomoo Mitsunaga. High dynamic range imaging: Spatially varying pixel exposures. In *Proceedings IEEE Conference on Computer Vision and Pattern Recognition. CVPR 2000 (Cat. No. PR00662)*, volume 1, pages 472–479. IEEE, 2000.
- [47] Yuzhen Niu, Jianbin Wu, Wenxi Liu, Wenzhong Guo, and Rynson WH Lau. Hdr-gan: Hdr image reconstruction from multi-exposed ldr images with large motions. *IEEE Transactions on Image Processing*, 30:3885–3896, 2021.

- [48] Feiyue Peng, Maojun Zhang, Shiming Lai, Hanlin Tan, and Shen Yan. Deep hdr reconstruction of dynamic scenes. In *2018 IEEE 3rd International Conference on Image, Vision and Computing (ICIVC)*, pages 347–351. IEEE, 2018.
- [49] K Ram Prabhakar, Susmit Agrawal, Durgesh Kumar Singh, Balraj Ashwath, and R Venkatesh Babu. Towards practical and efficient high-resolution hdr deghosting with cnn. In *Computer Vision–ECCV 2020: 16th European Conference, Glasgow, UK, August 23–28, 2020, Proceedings, Part XXI 16*, pages 497–513. Springer, 2020.
- [50] K Ram Prabhakar, Rajat Arora, Adhitya Swaminathan, Kunal Pratap Singh, and R Venkatesh Babu. A fast, scalable, and reliable deghosting method for extreme exposure fusion. In *2019 IEEE International Conference on Computational Photography (ICCP)*, pages 1–8. IEEE, 2019.
- [51] Henri Rebecq, René Ranftl, Vladlen Koltun, and Davide Scaramuzza. High speed and high dynamic range video with an event camera. *IEEE transactions on pattern analysis and machine intelligence*, 43(6):1964–1980, 2019.
- [52] Pradeep Sen, Nima Khademi Kalantari, Maziar Yaesoubi, Soheil Darabi, Dan B Goldman, and Eli Shechtman. Robust patch-based hdr reconstruction of dynamic scenes. *ACM Trans. Graph.*, 31(6):203–1, 2012.
- [53] Yong Shu, Liquan Shen, Xiangyu Hu, Mengyao Li, and Zihao Zhou. Towards real-world hdr video reconstruction: A large-scale benchmark dataset and a two-stage alignment network. In *Proceedings of the IEEE/CVF Conference on Computer Vision and Pattern Recognition*, pages 2879–2888, 2024.
- [54] Steven Tel, Zongwei Wu, Yulun Zhang, Barthelemy Heyrman, Cedric Demonceaux, Radu Timofte, and Dominique Ginhac. Alignment-free hdr deghosting with semantics consistent transformer. In *2023 IEEE/CVF International Conference on Computer Vision (ICCV)*, pages 12790–12799. IEEE Computer Society, 2023.
- [55] Michael D Tocci, Chris Kiser, Nora Tocci, and Pradeep Sen. A versatile hdr video production system. *ACM Transactions on Graphics (TOG)*, 30(4):1–10, 2011.
- [56] Caixin Wang, Jie Zhang, Matthew A Wilson, and Ralph Etienne-Cummings. Pix2hdr-a pixel-wise acquisition and deep learning-based synthesis approach for high-speed hdr videos. *IEEE Transactions on Pattern Analysis and Machine Intelligence*, 46(12):8771–8787, 2024.
- [57] Lin Wang and Kuk-Jin Yoon. Deep learning for hdr imaging: State-of-the-art and future trends. *IEEE Transactions on Pattern Analysis and Machine Intelligence*, 44(12):8874–8895, 2021.
- [58] Yue Wang, Tingting Jiang, Siwei Ma, and Wen Gao. Spatio-temporal ssim index for video quality assessment. In *2012 Visual Communications and Image Processing*, pages 1–6. IEEE, 2012.
- [59] Zhou Wang, Alan C Bovik, Hamid R Sheikh, and Eero P Simoncelli. Image quality assessment: from error visibility to structural similarity. *IEEE transactions on image processing*, 13(4):600–612, 2004.
- [60] GuanJun Wu, Taoran Yi, Jiemin Fang, Wenyu Liu, and Xinggong Wang. Fast high dynamic range radiance fields for dynamic scenes. *arXiv preprint arXiv:2401.06052*, 2024.
- [61] Shangzhe Wu, Jiarui Xu, Yu-Wing Tai, and Chi-Keung Tang. End-to-end deep hdr imaging with large foreground motions. In *European Conference on Computer Vision*, volume 1, 2018.
- [62] Gangwei Xu, Yujin Wang, Jinwei Gu, Tianfan Xue, and Xin Yang. Hdrflow: Real-time hdr video reconstruction with large motions. In *Proceedings of the IEEE/CVF Conference on Computer Vision and Pattern Recognition*, pages 24851–24860, 2024.
- [63] Tianfan Xue, Baian Chen, Jiajun Wu, Donglai Wei, and William T Freeman. Video enhancement with task-oriented flow. *International Journal of Computer Vision*, 127(8):1106–1125, 2019.
- [64] Qingsen Yan, Weiye Chen, Song Zhang, Yu Zhu, Jinqiu Sun, and Yanning Zhang. A unified hdr imaging method with pixel and patch level. In *Proceedings of the IEEE/CVF Conference on Computer Vision and Pattern Recognition*, pages 22211–22220, 2023.
- [65] Qingsen Yan, Dong Gong, Qinfeng Shi, Anton van den Hengel, Chunhua Shen, Ian Reid, and Yanning Zhang. Attention-guided network for ghost-free high dynamic range imaging. In *Proceedings of the IEEE/CVF Conference on Computer Vision and Pattern Recognition*, pages 1751–1760, 2019.
- [66] Qingsen Yan, Bo Wang, Lei Zhang, Jingyu Zhang, Zheng You, Qinfeng Shi, and Yanning Zhang. Towards accurate hdr imaging with learning generator constraints. *Neuro-computing*, 428:79–91, 2021.
- [67] Qingsen Yan, Kangzhen Yang, Tao Hu, Genggeng Chen, Kexin Dai, Peng Wu, Wenqi Ren, and Yanning Zhang. From dynamic to static: Stepwisely generate hdr image for ghost removal. *IEEE Transactions on Circuits and Systems for Video Technology*, 2024.
- [68] Wei Zhang and Wai-Kuen Cham. Gradient-directed multiexposure composition. *IEEE Transactions on Image Processing*, 21(4):2318–2323, 2011.
- [69] Zhengyou Zhang. A flexible new technique for camera calibration. *IEEE Transactions on Pattern Analysis and Machine Intelligence*, 22(11):1330–1334, 2002.
- [70] Hang Zhao, Boxin Shi, Christy Fernandez-Cull, Sai-Kit Yeung, and Ramesh Raskar. Unbounded high dynamic range photography using a modulo camera. In *2015 IEEE International Conference on Computational Photography (ICCP)*, pages 1–10. IEEE, 2015.
- [71] Bolun Zheng, Xiaokai Pan, Hua Zhang, Xiaofei Zhou, Gregory Slabaugh, Chenggang Yan, and Shanxin Yuan. Domainplus: Cross transform domain learning towards high dynamic range imaging. In *Proceedings of the 30th ACM International Conference on Multimedia*, pages 1954–1963, 2022.
- [72] Bolun Zheng, Shanxin Yuan, Chenggang Yan, Xiang Tian, Jiyong Zhang, Yaoqi Sun, Lin Liu, Aleš Leonardis, and Gregory Slabaugh. Learning frequency domain priors for image demoiring. *IEEE Transactions on*

Pattern Analysis and Machine Intelligence, 44(11):7705–7717, 2021.